Nanoshell-mediated robust entanglement between coupled quantum dots

Jabir Hakami[*] and M. Suhail Zubairy[†]

Institute for Quantum Science and Engineering and Department of Physics and Astronomy, Texas A&M University,
College Station, Texas 77843, USA

The exact entanglement dynamics in a hybrid structure consisting of two quantum dots (QDs) in the proximity of a metal nanoshell is investigated. Nanoshells can enhance the local density of states, leading to a strong-coupling regime where the excitation energy can coherently be transferred between the QDs and the nanoshell in the form of Rabi oscillations. The long-lived entangled states can be created deterministically by optimizing the shell thickness as well as the ratio of the distances between the QDs and the surface of the shell. The loss of the system is greatly reduced even when the QDs are ultraclose to the shell, which signifies a slow decay rate of the coherence information and longtime entanglement preservation. Our protocol allows for an on-demand, fast, and almost perfect entanglement even at strong carrier-phonon interaction where other systems fail.

I. INTRODUCTION

Conducting nanostructures at optical frequencies have long held the promise for multiple technological applications. Such structures have recently received considerable interest due to their potential in achieving strong, coherent coupling between individual emitters and electromagnetic excitations via excitation of plasmons localized to nanoscale dimensions. This strong coupling is possible due to the small mode volume associated with the subwavelength surface-plasmonic confinement [1–4]. By confining the light in nanoscale volumes, various interesting plasmonic elements allow, for example, for a nanoscale realization of the Mollow triplet of emission spectra [5,6] and nonclassical photon correlations between the emissions from the quantum dot and the ends of the nanowire [7]. Furthermore, plasmon-enhanced photocatalytic activity has been investigated experimentally in the spirit of the interplay of a coupled nanocomposite system consisting of a quantum dot (QD) and a metal nanoparticle (MNP) [8]. Also, the interplay and modification of the photoexcitation processes in a hybrid system composed of QD and MNP is treated self-consistently [9] by applying the theoretical work reported in [10]. In addition, integrating semiconductor QDs with a MNP provides useful means to couple light and matter. This coupling can be enhanced tremendously by placing QDs in proximity to a nanostructured optical environment that enables strong confinement of light and thus increases the light-matter interaction. Remarkably, QDs offer many advantages over atomic systems, including the small size and large optical dipole moments and transition energies, and they can be positioned deterministically and remain stationary without requiring atom traps [11–13].

One of the fascinating applications of these nanostructures is their ability to generate entangled states of a two-qubit system. It has been demonstrated that semiconducting QDs are promising candidates for the basic device units for quantum information processing [14,15]. Fundamentally, a strong light-matter interaction is a prerequisite to generate entanglement between quantum bits (qubits) for optical quantum information systems. Recently, the entanglement dynamics in a system consisting of two identical quantum emitters in the vicinity

of a solid-sphere MNP was investigated [16,17]. However, in these models the MNPs are treated in a quasistatic approximation in which the contribution of retardation effects is ignored. Also, while the spherical MNP has a simpler structure, the plasmon resonance appears at higher frequencies where the contribution of the interband absorption is magnified, thus leading to a fast decay of entanglement. On the other hand, nanoshells with extraordinary properties support surface plasmon resonances (SPRs) that are highly geometric dependent (their resonance frequencies depend significantly on the shell thickness), and they respond more sensitively to the changes in the environment [18–20]. This leads to a structure that has extraordinary properties.

In the present work, we study the entanglement generation in a hybrid structure consisting of two QDs in the vicinity of a metal nanoshell. The entanglement arises impulsively due to common coupling to the plasmonic nanostructure, without demanding postselective measurement or mediating the dissipative environment. We use a self-consistent photon Green's-function technique to explore the quantum optical and entanglement dynamics between two QDs that cover all the coupling regimes. We demonstrate that the QDs, which are resonantly coupled to the nanoshell with only one being initially excited, can form a coherent superposition state significantly faster than the losses in the system. We have found that the long-lived entangled state depends perceptively on the shell thickness as well as on the ratio of the distances between the two QDs and the surface of the shell. Contrary to a nanosphere, the entanglement mediated by a nanoshell is robust even when the dephasing rate and the detuning between the transition frequencies of the two QDs are rigorously included.

The organization of this paper is as follows. In Sec. II A, we present the theoretical model for the hybrid system. In Sec. II B, we study the enhancement of the local density of states in the proximity of the nanoshell. In Sec. III, we calculate and discuss the results of the concurrence of two QDs in a homogeneous background, coupled by the nanoshell localized surface plasmon. Our conclusion is presented in Sec. IV

II. THEORETICAL FRAMEWORK

A. Model and Hamiltonian

The hybrid system consisting of two QDs in the proximity of a metal nanoshell is schematically presented in Fig. 1. The

---
[*]jhakami@physics.tamu.edu
[†]zubairy@physics.tamu.edu
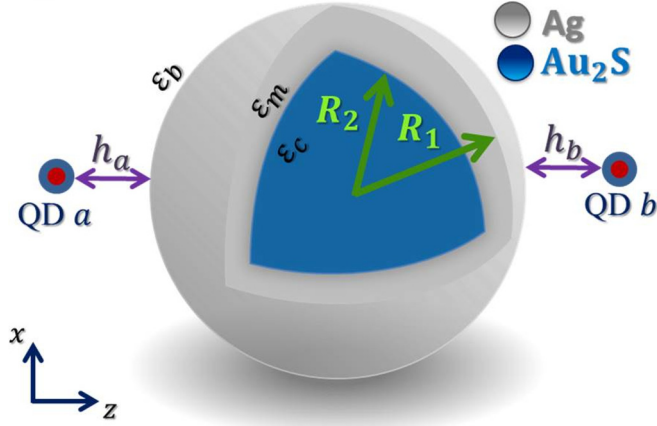
FIG. 1. Schematic diagram of the hybrid system consisting of two QDs, labeled QD a and QD b, located at different distances $r_a = R_1 + h_a$ and $r_b = R_1 + h_b$ from the center of a Au$_2$S/Ag nanoshell. The QD-nanoshell system is embedded in a homogeneous background medium with permittivity ϵ_b. The Au$_2$S core has radius R_2 and dielectric constant ϵ_c. The concentric Ag shell has a total nanoparticle radius R_1 and permittivity $\epsilon_m(\omega)$.

QDs labeled, QD a and QD b, are located at distances h_a and h_b with respect to the surface of the metallic shell. Unless stated otherwise, the structure of the nanoshell is modeled as a spherical Au$_2$S core of radius R_2 and permittivity $\epsilon_c = 5.4$ [21]. Surrounding the Au$_2$S core is a concentric Ag shell of $d = R_1 - R_2$ with a frequency-dependent dielectric permittivity $\epsilon_m(\omega)$ taken from Ref. [22]. Here, R_1 is the external radius of the shell. The core-shell system is entrenched in an aqueous medium of dielectric constant $\epsilon_b = 1.78$ [21]. The distances from QD a and QD b to the center of the nanoshell are $r_a = R_1 + h_a$ and $r_b = R_1 + h_b$, respectively. The QDs are treated as two-level systems for resonant excitation of the energetically lowest electronic transition between valence- and conduction-band states. The methodology to map the full many-body problem on a discrete energy-level scheme for the strongly confined excitons is advocated by numerous theoretical and experimental studies [14,23–28]. Each QD is modeled as a two-level system with the optical transition frequency ω_i for the ith QD, internal nonradiative decay rate γ'_i, and the transition dipole moment $\boldsymbol{d}_i$.

The size-dependent dielectric function due to the finite-size effect of the nanoparticle can be accounted for empirically using the "limited mean-free-path model" [29]. In this model, the damping constant is given by $\Gamma = \Gamma_{\text{bulk}} + A\upsilon_F / \ell$, where Γ_{bulk} is the damping constant for the bulk, $\upsilon_F = 1.39 \times 10^8$ cm/s is the Fermi velocity of the conduction electrons in the silver, and ℓ is the characteristic dimension depending on the geometry of the nanoparticle, which is in our model proportional to the thickness of the nanoshell. The constant A depends on the nanoparticle shape and on the theory. The best agreement with the experiments is found for $A = 0.25$ [30]. Here, the frequency-dependent dielectric function of the silver nanoshell including the size effect can be expressed as [29]

$$\epsilon_m(\omega, d) = \epsilon_{\text{exp}}(\omega) + \frac{\omega_p^2}{\omega^2 + i\omega\Gamma_{\text{bulk}}} - \frac{\omega_p^2}{\omega^2 + i\omega\Gamma}, \quad (1)$$

where $\omega_p = 1.3987 \times 10^{16}$ s^{-1} is the bulk plasmon frequency and $\Gamma_{\text{bulk}} = 0.03 \times 10^{15}$ s^{-1} is the bulk collision frequency of conduction electrons in silver. $\epsilon_{\text{exp}}(\omega)$ is the experimental frequency-dependent dielectric function taken from Ref. [22].

To scrutinize the strong-coupling case, we adopt a macroscopic QED formalism [4,31] for calculating the entanglement of coupled QDs in a lossy, nonhomogeneous environment. It relies on the diagonalization of a Hamiltonian that includes the coupled QDs, the electromagnetic modes of the nanoshell metal nanoparticle, including their inherent losses, and the light-matter coupling by means of a dipolar interaction,

$$\hat{H} = \int d\boldsymbol{r} \int_0^\infty d\omega \hbar\omega \hat{\boldsymbol{f}}^\dagger(\boldsymbol{r}, \omega) \cdot \hat{\boldsymbol{f}}(\boldsymbol{r}, \omega) + \sum_{i=a,b} \frac{\hbar\Omega_i}{2} \hat{\sigma}_i^z$$
$$- \sum_{i=a,b} \int_0^\infty d\omega [[\hat{\sigma}_i^- + \hat{\sigma}_i^+] \boldsymbol{d}_i \cdot \hat{\boldsymbol{E}}(\boldsymbol{r}_i, \omega) + \text{H.c.}], \quad (2)$$

where $\Omega_i = \omega_i - i\gamma'_i/2$. Here, $\hat{\boldsymbol{f}}(\boldsymbol{r}, \omega)$ is the bosonic vector field annihilation operator for the elementary excitations of the system. The QDs are described in terms of the fermionic operators $\hat{\sigma}_i$. The first and the second terms shown in Eq. (2) describe the noninteracting Hamiltonian of the total electromagnetic field and the energy of the QDs, respectively. The third term illustrates the interaction energy between QDs and the excitation of surface plasmon at the QDs locations.

The electric field is quantized by introducing the media as phenomenological noise currents that are associated with the electric and magnetic losses due to material absorption in Maxwell's equations, and the field operators are obtained indirectly from the noise operators via the classical Green's function. The electric field operator at the position of the QD is given by [31]

$$\hat{\boldsymbol{E}}(\boldsymbol{r}, \omega) = i\sqrt{\frac{\hbar}{\pi\epsilon_0}} \int d\boldsymbol{r}' \frac{\omega^2}{c^2}$$
$$\times \sqrt{\epsilon_I^m(\boldsymbol{r}', \omega)} \boldsymbol{G}(\boldsymbol{r}, \boldsymbol{r}', \omega) \hat{\boldsymbol{f}}(\boldsymbol{r}', \omega), \quad (3)$$

where ϵ_I^m is the imaginary part of the complex dielectric function $\epsilon_m(\boldsymbol{r}, \omega) = \epsilon_R^m(\boldsymbol{r}, \omega) + i\epsilon_I^m(\boldsymbol{r}, \omega)$. Here, $\boldsymbol{G}(\boldsymbol{r}, \boldsymbol{r}', \omega)$ is the frequency-dependent electromagnetic Green's function, describing the system response at $\boldsymbol{r}$ to a point source at $\boldsymbol{r}'$:

$$\left[\boldsymbol{\nabla} \times \boldsymbol{\nabla} \times -\frac{\omega^2}{c^2}\epsilon_m(\boldsymbol{r}, \omega) \right] \boldsymbol{G}(\boldsymbol{r}, \boldsymbol{r}', \omega) = \boldsymbol{I}\delta(\boldsymbol{r} - \boldsymbol{r}'), \quad (4)$$

where $\boldsymbol{I}$ is the unit dyadic. In this hybrid system, the direct dipole-dipole interactions are naturally included in the total Green's function.

Before closing this theory section, we highlight that our general approach can be adapted beyond the dipole approximation in order to include nondipole effects for the QDs using the same Green's function introduced above [13,32,33]. Nonetheless, the dipole approximation is justified for strongly confined dots where the higher-lying energy levels become substantially separated [27,34]. We have found that the near field is distributed uniformly over a small volume of QDs, showing good agreement with the results reported in Ref. [27]. Additionally, Kristensen *et al.* [35] have verified that the Purcell effect is independent of the size of the wave function for

the case of spherically symmetric exciton wave functions, i.e., is determined only by the photonic response in the center of the emitter. For a practical application, their exact calculations have been confirmed by computing the Purcell factor for a spherical QD near a silver metal, and the conclusion is that the results coincide with the dipole approximation and there is no spatial averaging of the local density of states across the volume of the QD, in spite of the large field gradients near the metal in their structure. It is meaningful to compare this to the experimental results reported in Ref. [13] where the dipole approximation failed for relatively small self-assembled QDs. That is because, for simplicity, we consider only heavy-hole transitions and leave the modeling of strained QDs for future studies.

B. Modified spontaneous emission dynamics

We consider the decay dynamics of the two coupled QDs that have states a and b as their respective upper excited level. The initial field is assumed to be in vacuum; thus all the resultant dynamics in this system will be driven by the initial excitation of QDs. We assume that, at most, one QD is excited at any time. Thus a possible initial condition is that the QD system is in the state $|\psi(t=0)\rangle = C_a(0)|U_a\rangle + C_b(0)|U_b\rangle$, where $|U_a\rangle \equiv |1\rangle_a|0\rangle_b$ and $|U_b\rangle \equiv |0\rangle_a|1\rangle_b$, which can be prepared through appropriate optical or electronic excitation of the solid-state QD system. Here, $|0\rangle_i$ and $|1\rangle_i$ represent the ith QD in the ground and excited states, respectively.

The time evaluation for this initial state is given by

$$|\psi(t)\rangle = \sum_i C_i(t) e^{-i(\Omega_i - \overline{\Omega})t}|U_i\rangle|0\rangle$$
$$+ \int d\mathbf{r} \int_0^\infty d\omega C_L(\mathbf{r},\omega,t) e^{-i(\omega - \overline{\Omega})t}|L\rangle|\mathbf{1}(\mathbf{r},\omega)\rangle, \tag{5}$$

where $|\mathbf{1}(\mathbf{r},\omega)\rangle = \hat{\mathbf{f}}^\dagger(\mathbf{r},\omega)|\{0\}\rangle$, $|L\rangle$ is the state where both QDs are in the lower state, i.e., $|L\rangle = |0\rangle_a|0\rangle_b$, and $\overline{\Omega}$ is the average of the frequencies Ω_i, where in the case of $\gamma_i' = 0$, we have $\overline{\Omega} = \overline{\omega} \equiv \frac{1}{2}\sum_i \omega_i$ ($i = a$ or b).

The time-dependent Schrödinger equation in the rotating-wave approximation leads to the following equation of motion for the probability amplitudes:

$$\dot{C}_i(t) = -\frac{1}{\sqrt{\hbar\pi\epsilon_0}} \int_0^\infty d\omega \frac{\omega^2}{c^2} \int d\mathbf{r} \sqrt{\epsilon_I(\mathbf{r},\omega)}$$
$$\times \mathbf{d}_i^* \cdot \mathbf{G}(\mathbf{r}_i,\mathbf{r},\omega) C_L(\mathbf{r},\omega,t) e^{-i(\omega - \Omega_i)t}, \tag{6}$$

$$\dot{C}_L(\mathbf{r},\omega,t) = \frac{1}{\sqrt{\hbar\pi\epsilon_0}} \frac{\omega^2}{c^2} \sqrt{\epsilon_I(\mathbf{r},\omega)}$$
$$\times \sum_j \mathbf{d}_j \cdot \mathbf{G}^*(\mathbf{r}_j,\mathbf{r},\omega) C_j(t) e^{i(\omega - \Omega_j)t}, \tag{7}$$

where we assumed for the pure dephasing rate $\gamma_i' = \gamma_{a/b}'$. Integrating Eq. (7) and substituting into Eq. (6), we obtain the integro-differential equations for the probability amplitudes $C_i(t)$. Introducing the kernel function $K_{r_i r_j}(t,t')$, these two

equations can be rewritten as

$$\dot{C}_a(t) = -\int_0^t dt' [K_{r_a r_a}(t,t') C_a(t') + K_{r_a r_b}(t,t') C_b(t')], \tag{8a}$$

$$\dot{C}_b(t) = -\int_0^t dt' [K_{r_b r_b}(t,t') C_b(t') + K_{r_b r_a}(t,t') C_a(t')], \tag{8b}$$

where the kernel function

$$K_{r_i r_j}(t,t') = \frac{1}{\hbar\pi\epsilon_0} \int_0^\infty d\omega e^{-i(\omega - \Omega_i)t} e^{i(\omega - \Omega_j)t'}$$
$$\times \mathbf{d}_i^* \cdot \left\{ \frac{\omega^2}{c^2} \text{Im}[\mathbf{G}(\mathbf{r}_i,\mathbf{r}_j,\omega)] \right\} \cdot \mathbf{d}_j$$
$$= \int_0^\infty d\omega J_{ij}(\omega) e^{-i(\omega - \Omega_i)t} e^{i(\omega - \Omega_j)t'} \tag{9}$$

($i,j = a$ or b). Taking the time integral of both sides of Eqs. (8) leads to the well-known Volterra integral equations of the second kind [36].

Here, the action of the dissipative medium depicted in Fig. 1 on the ith QD is described by the so-called spectral density [37] defined as

$$J_{ii}(\omega) = \frac{1}{\hbar\pi\epsilon_0} \mathbf{d}_i^* \cdot \left\{ \frac{\omega^2}{c^2} \text{Im}[\mathbf{G}(\mathbf{r}_i,\mathbf{r}_i,\omega)] \right\} \cdot \mathbf{d}_i. \tag{10}$$

This expression can be expressed in terms of the electromagnetic density of states as

$$J_{ii}(\omega) = \frac{1}{2} \frac{\omega}{3\hbar\epsilon_0} |\mathbf{d}_i|^2 \rho(\mathbf{r}_i,\omega), \tag{11}$$

where $\rho(\mathbf{r}_i,\omega)$ is the local density of states expressed in terms of the system's dyadic Green's function as

$$\rho(\mathbf{r}_i,\omega) = \frac{6\omega}{\pi c^2} \{\mathbf{n}_p \cdot \text{Im}[\mathbf{G}(\mathbf{r}_i,\mathbf{r}_i,\omega)] \cdot \mathbf{n}_p\}, \tag{12}$$

where $\mathbf{n}_p$ is a unit vector pointing in the direction of $\mathbf{p}$. The enhancement of the projected local density of states, in the direction $\mathbf{n}_p$, is defined as

$$F_{\mathbf{n}_p}(\omega) = \frac{\mathbf{n}_p \cdot \text{Im}[\mathbf{G}(\mathbf{r}_i,\mathbf{r}_i,\omega)] \cdot \mathbf{n}_p}{\mathbf{n}_p \cdot \text{Im}[\mathbf{G}^0(\mathbf{r}_i,\mathbf{r}_i,\omega)] \cdot \mathbf{n}_p}, \tag{13}$$

where $\text{Im}[\mathbf{G}^0(\mathbf{r}_i,\mathbf{r}_i,\omega)] = \frac{k_1}{6\pi}\mathbf{I}$ is the imaginary part of the homogeneous Green's tensor. Here, $k_1 = \omega\sqrt{\epsilon_b}/c$, where ϵ_b is the dielectric constant of the surrounding medium. In this case, all the matter parameters that are relevant to the geometrical and material information are directly included in the Green's function. The plasmon resonance can be obtained by including the retardation effect from the explicit form of the reflection coefficients derived in Appendix A by noticing that these coefficients contain poles at the points where the denominator vanishes. These poles give the eigenfrequency relation of the electric modes supported by the metallic shell. The detail derivations are given in Appendix B.

The enhancement of the z-projected local density of states $F_z(\omega)$ for a QD exciton located at $\mathbf{r}_{a/b} = 19\hat{\mathbf{e}}_z$ from the center of the Au$_2$S/Ag nanoshell is shown in Fig. 2(a). The plasmon resonance peaks can be obtained analytically from the solutions of the eigenfrequency relation given in Appendix B [see Eq. (B1)]. Each mode splits into two modes, cavitylike ω_{n+} at high frequencies (antisymmetric SPR modes)
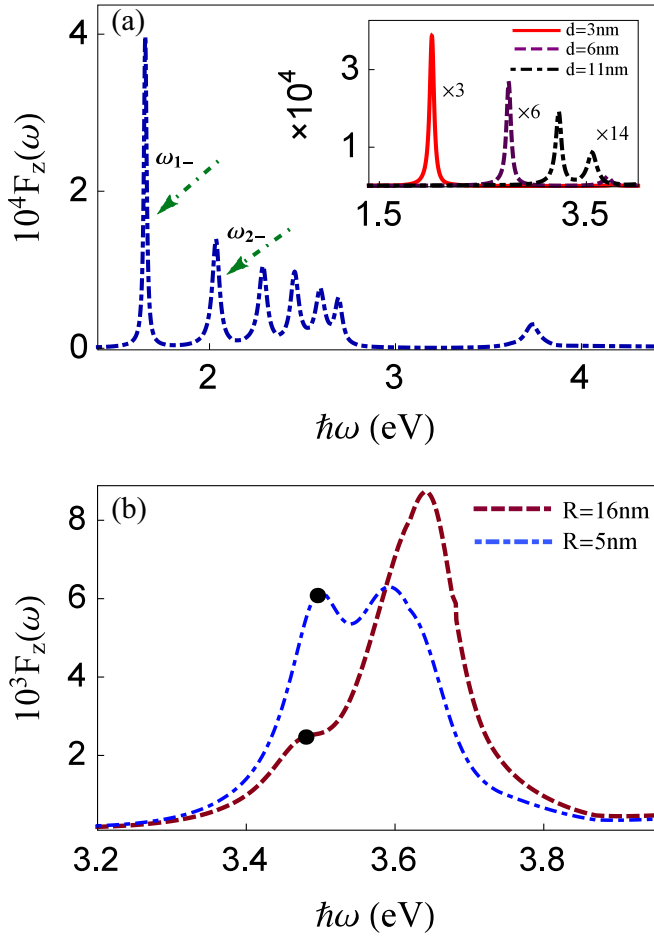
FIG. 2. (a) Enhancement of z-projected local density of states, $\hat{e}_z \cdot \text{Im}[\boldsymbol{G}(\boldsymbol{r}_{a/b}, \boldsymbol{r}_{a/b}, \omega)] \cdot \hat{e}_z$ in units of $\hat{e}_z \cdot \text{Im}[\boldsymbol{G}^0(\boldsymbol{r}_{a/b}, \boldsymbol{r}_{a/b}, \omega)] \cdot \hat{e}_z$ calculated at $h_{a/b} = 3$ nm from the surface of a Au$_2$S/Ag nanoshell. The Au$_2$S core has radius $R_2 = 14$ nm and refractive index $n_c^2 \equiv \epsilon_c = 5.4$. The concentric shell has a total radius $R_1 = 16$ nm and frequency-dependent permittivity $\epsilon_m(\omega, d)$ given in the text. Inset: The dependence of the plasmon resonance on the shell thickness (in the dipole approximation): $d = 3$ nm (solid red curve), 6 nm (dashed purple curve), and $d = 11$ nm (dash-dotted black curve). (b) Enhancement of z-projected local density of states calculated at $h_{a/b} = 3$ nm from the surface of a Ag solid-sphere nanoparticle with different radii: $R = 16$ nm (dashed red curve) and $R = 5$ nm (dash-dotted blue curve). Here, $\epsilon_c \equiv \epsilon_m(\omega) = \epsilon_m(\omega, R)$. The locations of the localized SPRs are indicated by superimposed black dots on the curves.

converging to $\sum_n \omega_{n+}$ and spherelike ω_{n-} modes at low frequencies (symmetric SPR modes). The splitting originates from the hybridization or coupling of plasmons bound to different (internal and external) surfaces of the shell. In Fig. 2(a), the low-frequency modes ω_{n-} are shown explicitly, and the converged high-frequency modes $\sum_n \omega_{n+}$ are shown as the peak on the right. This doublet structure of optical spectra of metallic shells has been demonstrated theoretically and observed experimentally [29]. Remarkably, the localized SPR in our structure appears at low frequency around 1.6 eV, which is close to the wavelengths that have potential applications in biomedicine, in optical communication, and for many QD
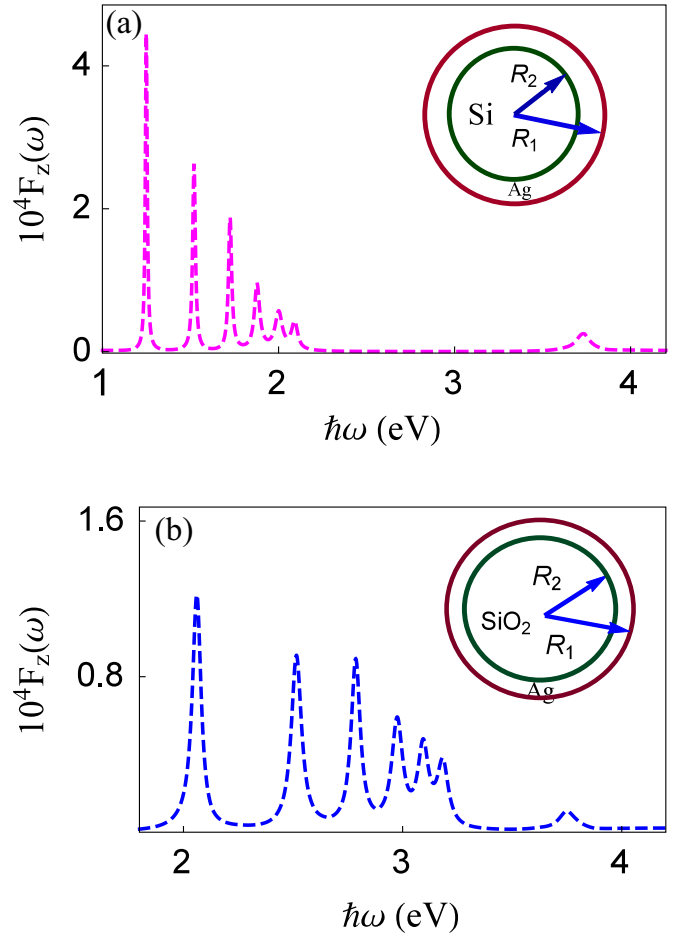
FIG. 3. Enhancement of z-projected local density of states, $\hat{e}_z \cdot \text{Im}[\boldsymbol{G}(\boldsymbol{r}_{a/b}, \boldsymbol{r}_{a/b}, \omega)] \cdot \hat{e}_z$ in units of $\hat{e}_z \cdot \text{Im}[\boldsymbol{G}^0(\boldsymbol{r}_{a/b}, \boldsymbol{r}_{a/b}, \omega)] \cdot \hat{e}_z$ calculated at $h_{a/b} = 3$ nm from the surface of (a) a Si/Ag nanoshell and (b) a SiO$_2$/Ag nanoshell. The spherical silicon core, Si, has radius $R_2 = 14$ nm and refractive index $n_c = 3.42$ [38], while the spherical silica core, SiO$_2$, has radius $R_2 = 14$ nm and refractive index $n_c = 1.46$ [39]. The concentric shell, Ag, has a total radius $R_1 = 16$ nm and the same permittivity $\epsilon_m(\omega, d)$ given in Fig. 2. Inset: Sketch of the shell-core nanoparticle with different core materials.

emitters. The appearance of this resonance frequency in the near infrared, where the losses of the metal silver are at a minimum, results in a spectral width, i.e., the FWHM, of only 18 meV [see Fig. 2(a)]. Interestingly, the inverse of the linewidth of the nanoparticle plasmon is directly proportional to the field strength at the surface of the nanoshell. The dependence of the localized SPR on the shell thickness is shown (in the dipole approximation) in the inset of Fig. 2(a). These results show the strong sensitivity of the plasmon resonance to the shell thickness, although the outer radius is fixed at 16 nm. In addition, the interband contribution diminishes the intensity of the SPR if it occurs at wavelengths shorter than the threshold wavelength. This explains the lower intensities for shell thickness $d = 11$ nm (dash-dotted black curve) than for $d = 3$ nm (solid red curve).

In Fig. 2(b) we demonstrate the enhancement of the z-projected local density of states $F_z(\omega)$ for the case of a

solid-sphere nanoparticle with different sizes: $R = 16$ nm (dashed red curve) and $R = 5$ nm (dash-dotted blue curve). This is a consequence of the fact that when $\epsilon_c \equiv \epsilon_m(\omega) = \epsilon_m(\omega, R)$, the coefficients of the shell-core nanoparticle [see Eqs. (A8)–(A11)] reduces to those of a solid sphere with radius R_1. The locations of the localized SPRs are indicated by black dots superimposed on the curves. In contrast to the nanoshell [Fig. 2(a)], the localized SPRs for the solid sphere occur at higher frequencies near 350 nm, where the interband absorption is magnified [21,23]. Additionally, the corresponding localized SPR is redshifted slightly and broadened with increasing size of the nanoparticle. In this case, the contribution of the retardation effects dominates, and the reservoir function $\rho(\mathbf{r}_i, \omega)$ cannot be described by a single Lorentzian line shape.

In Fig. 3, we exemplify the dependence of the local density of states on the geometrics of the nanoshell. Here, Eq. (13) is calculated numerically for two different core materials: (a) Si with the highest refractive index [38] and (b) SiO$_2$ with the lowest refractive index [39]. Recently, it was established that the silicon-silver (Si-Ag) interface is significantly important in industrial solar cells, and understanding and tailoring the metal-semiconductor interface is practically important in all semiconductor devices [40]. In Fig. 3(a), we show that the silicon core can significantly influence the optical properties of the metal nanoshell. The localized SPR peak is considerably redshifted, and the FWHM becomes very narrow. Thus, increasing the core dielectric constant increases nanoparticle absorption efficiency, reduces plasmon linewidth, and adjusts plasmon energies. These results agree very well with the elaborate experiment reported in Ref. [41]. This is encouraging because the results show that even the higher-order modes such as quadrupole SPR become practically useful due to significantly low losses. This leads to a structure that has extraordinary prop-

erties. This is in contrast to the results shown in Fig. 3(b) for the SiO$_2$ core, where the linewidth is enlarged and losses as a result of the contributions of the higher-order modes become severe.

III. RESULTS AND DISCUSSION

In this section, we have numerically solved the time-dependent dynamical equations (8) motivated by the results in Figs. 2 and 3 to demonstrate the decay evolutions of the QD excitons and the corresponding entanglement with QD a being initially excited, i.e., with the initial wave function $|\psi(t = 0)\rangle = |1\rangle_a |0\rangle_b$. The population dynamics is exact as we have performed neither the Born nor the Markov approximation. For all numerical calculations, we have considered parameters from a single-QD optical experiment with optical dipole moment $d_{a/b} = d_0 = 60$ D [42]. In addition, we assume the pure dephasing rate $\gamma_i' = \gamma_{a/b}' = 1 \mu$eV (equal for all QDs) as demonstrated in recent experiments for the decay of InAs QDs at room temperature [43,44]. Note that even for a larger rate of $\gamma' = 1$ meV, the numerical results are essentially identical since the plasmon coupling completely dominates the decay.

The quantum entanglement of a two-qubit system can be well quantified by the concurrence $\mathcal{C}(t)$, ranging from zero for separable states up to 1 for maximally entangled states, which is given by [45]

$$\mathcal{C}(\rho) = \max\{0, \lambda_1 - \lambda_2 - \lambda_3 - \lambda_4\}, \qquad (14)$$

where $\lambda_i(i = 1,2,3,4)$ are the eigenvalues, in descending order, of the Hermitian matrix $\Lambda = \sqrt{\sqrt{\rho_{ab}} \tilde{\rho}_{ab} \sqrt{\rho_{ab}}}$. The spin-flip density matrix is defined as $\tilde{\rho}_{ab} = (\sigma_y \otimes \sigma_y) \rho_{ab}^* (\sigma_y \otimes \sigma_y)$, where σ_y is a Pauli matrix.

In the $\{|11\rangle, |10\rangle, |01\rangle, |00\rangle\}$ basis, the reduced density matrix for the QDs is determined by tracing out the plasmon mode, which can be calculated to be

$$\rho_{ab}(t) = \begin{pmatrix} 0 & 0 & 0 & 0 \\ 0 & |C_a(t)|^2 & C_a(t)C_b^*(t)e^{-i\Delta} & 0 \\ 0 & C_a^*(t)C_b(t)e^{i\Delta} & |C_b(t)|^2 & 0 \\ 0 & 0 & 0 & 1 - |C_a(t)|^2 - |C_b(t)|^2 \end{pmatrix}, \qquad (15)$$

where $\Delta = \omega_a - \omega_b$ is the difference (mismatch) of the transition energies of individual QDs. Hence for the density matrix given by Eq. (15), the concurrence takes the form $\mathcal{C}(t) = 2\max\{0, |C_a(t)C_b^*(t)|\}$.

To better discuss the dynamical evaluation of the entanglement, we consider the initial state $|\psi(t = 0)\rangle = C_a(0)|U_a\rangle + C_b(0)|U_b\rangle$, with $C_a(0) = \sqrt{\frac{1-s}{2}}$ and $C_b(0) = \sqrt{\frac{1+s}{2}}e^{i\phi}$, where $-1 \leqslant s \leqslant 1$.

In Fig. 4, we show the dynamics of coupled QDs located symmetrically with respect to the Au$_2$S/Ag nanoshell (i.e., with $r_a = r_b$) as a function of normalized time. Here, we have assumed $\gamma_p = \Gamma_{\text{bulk}}$. We found that when both QDs are on resonance with the localized surface plasmon mode (i.e., $\omega_{n=1}$) and due to the enhancement of the local density of states [$F_z(\omega) \geqslant 10^4$], the influence on the dynamic process of the QD-nanoshell interactions dominates. The existence of the Rabi oscillation in the decay profiles signifies the strong interaction between QDs in the proximity of the surface

plasmon nanoshell, consequently demonstrating that the decay dynamics contains the non-Markovian features. Figure 4 also demonstrates that the entangled state can be sped up due to the Purcell effect as well as due to dealing with a superradiant triplet state. The possibility of manipulating and speeding up the transition process might play a vital role in the future development of quantum information processing. The exciton occupations is driven into a superposition state, as shown in Fig. 4, which can be explained as follows. The oscillation of the initially excited QD creates plasmon excitation at the site of the metallic nanoshell. Subsequently, the strong medium-assisted photon exchange acting back on the QDs is $\pi/2$ phase shifted with respect to the field acting on the medium. This phase shift results in the redistribution of the energy of the initially excited QD, causing the system evolution towards the stable superposition state $(|1\rangle_a|0\rangle_b - |0\rangle_a|1\rangle_b)$. Consequently, the total field at the site of the nanoshell is quenched. The system sustains a stable superposition state until the retardation effects
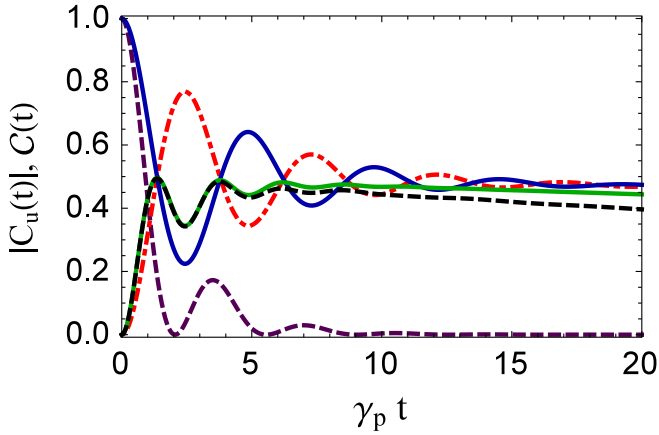
FIG. 4. The coupling dynamics (exciton occupations and concurrence) between coupled QDs for the case of $s = -1$ as a function of normalized time; the upper decay of the QDs a (solid blue curve) and b (dash-dotted red curve) and the concurrence (solid green curve). Here, $h_a = h_b = 3$ nm. The dashed black curve shows the entanglement with 3.6 meV detuning between the QDs. The population dynamics of QD a without QD b is shown in the dashed purple curve.

take place, which extract their energy in a nonradiative fashion. In this geometric arrangement, the entanglement oscillates $\sim$0.5, which is the maximum amount possible (solid green curve). For comparison, we show the dynamics of QD a in the absence of QD b, which displays a smaller oscillation and a faster decay (dashed purple curve) compared to the presence of QD b. In addition, we also calculate the entanglement with a realistic experimental energy mismatch when the detuning $\Delta = \omega_a - \omega_b$ of the transition energies between the QDs is equal to 3.6 meV (dashed black curve). The resulting concurrence is almost independent of Δ. This clearly indicates robustness of entanglement in our system.

The dipole asymmetry was also shown to offer a significant flexibility to derive quite different entanglement dynamics than the case of equal optical dipole moments by integrating planar-photonic-crystal (PPC) nanocavites with solid state [11]. However, the quality factor and the cavity mode volume in the latter system are always assumed to be very large, and subsequently reducing the quality factor in this system by one order of magnitude moves it to a weak-coupling regime [11]. Such difficulties can be avoided in our model, signifying the advantages of the nanoscale integration of metals and semiconductors.

In Fig. 5, we have investigated the non-Markovian decay dynamics of $|C_b(t)|$ for QD b initially in its ground state with the presence of the nanoshell modeled with different core materials. The oscillation dynamics is observable even with the significant metal losses. The results in Fig. 5 demonstrate the effects of the detuning on the excitation of QD b and subsequently the coupling of the system. Here, we have set $\omega_a = \omega_b = \omega_c + \Delta$, where ω_c is the SPR.

While for the Au$_2$S core QD b is excited at earlier times with pronounced oscillations, a small detuning of about or less than 6 meV results in slowing down the dynamics of the system (dash-double-dotted black curve). In contrast, for the SiO$_2$ core the oscillations for two cases [i.e., $\Delta = 0$ meV
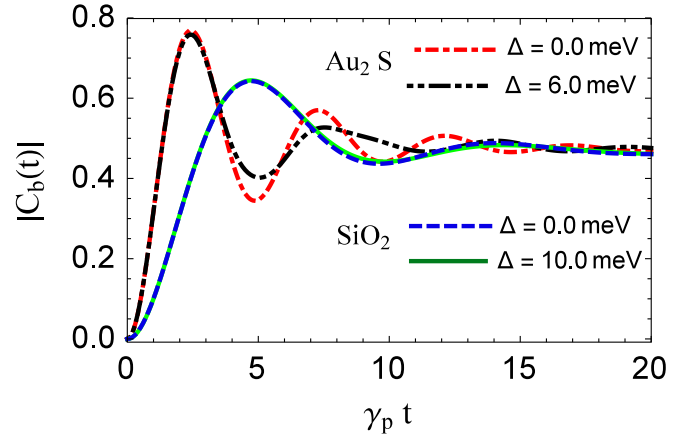
FIG. 5. Evaluation of the non-Markovian decay dynamics of QD b initially in the ground state as a function of normalized time with different core materials. Au$_2$S core: $\Delta = 0$ meV (dash-dotted red curve) and $\Delta = 6$ meV (dash-double-dotted black curve). SiO$_2$ core: $\Delta = 0$ meV (dashed blue curve) and $\Delta = 10$ meV (solid green curve). Here, $h_a = h_b = 3$ nm .

(dashed blue curve) and $\Delta = 10$ meV (solid green curve)] are identical, although the detuning is increased up to 10 meV. Thus the dynamics of the system are less dependent on the detuning if the losses are large and show strong sensitivity to the detuning if the losses are at the minimum.

In Fig. 6, we have looked at the effect of coherent exchange interaction in the presence of QDs pure dephasing. The concurrence shows rich dynamics, and the oscillations increased significantly with increasing γ', indicating that the two QDs are effectively coupled through the localized surface plasmon-induced photon exchange. The results in Fig. 6 clearly show the robustness of our protocol allows for an on-demand, fast, and almost perfect entanglement even at strong carrier-phonon interaction where other systems fail. In fact, the effectiveness of the presented schemes is shown to be better the stronger the carrier-phonon interaction is.
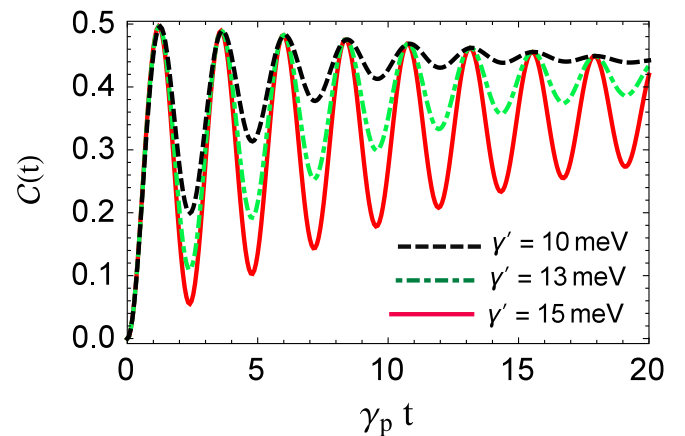
FIG. 6. The concurrence as a function of normalized time for the case of $s = -1$ with varying the QD pure dephasing: $\gamma' = 10$ meV (dashed black curve), $\gamma' = 13$ meV (dash-dotted green curve), and $\gamma' = 15$ meV (solid red curve). Here, $h_a = h_b = 3$ nm from the surface of the Au$_2$S/Ag.
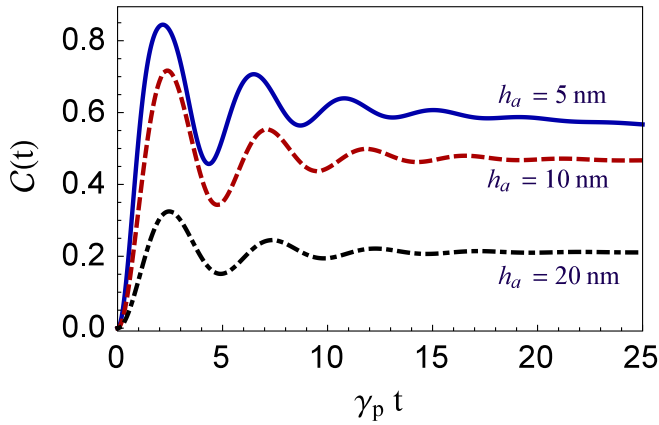
FIG. 7. The concurrence as a function of normalized time with $s = -1$ for various locations of QD a from the surface of Au$_2$S/Ag: $h_a = 5$ nm (solid blue curve), 10 nm (dashed red curve), and 20 nm (dash-dotted black curve). Here, $R_2/R_1 = 0.875$, and QD b is located 1 nm from the surface of the nanoshell.

Figure 7 shows the concurrence dependence on the asymmetry in the QD positions with respect to the nanoshell. Here, QD b is initially in the ground state and is situated very close to the surface of the nanoshell (i.e., $h_b = 1$ nm) while the location of the initially excited QD a is varied. While for the perfectly symmetric system shown in Fig. 4 the entanglement oscillates $\sim$0.5, which is the maximum amount possible, the results do already considerably change for slightly different QD locations: not only does the oscillation amplitude persist, but the system is efficiently coupled, and significantly higher entanglement is reached. For $h_b = 5$ nm, which turns out to be the optimal choice for the location of QD a, an ideal and robust entanglement is realized with $\mathcal{C}$ taking values of roughly 0.87. It is also found that the asymmetry in the QD positions with respect to the nanoshell leads to a steady-state entanglement existing for a sufficiently long time, in contrast to the symmetric case. These features indicate that the QD-nanoshell interaction enters the strong-coupling regime, where the excitation energy is coherently transferred between the QDs and the nanoshell in the form of Rabi oscillation. Eventually, when QD a is placed at large distances, the system enters a weak-coupling regime, and subsequently, the concurrence attains 0.35 as an optimum value (dash-dotted black curve). This is an exciting and promising result that can be implemented with current technology. This may lead to the design of devices at the nanoscale that may be useful for the quantum computing community.

The strong sensitivity of the entanglement to the shell thickness is shown in Fig. 8. The distances from QD a and QD b to the surface of the Au$_2$S/Ag nanoshell are 5 and 1 nm, respectively. The transition frequencies of the QDs are set to be resonant with the localized spherelike plasmon mode for different thicknesses of the shell. As the shell thickness increases, the plasmon resonance exhibits a large spectral shift to the higher frequencies [see the inset in Fig. 2(a)]. Additionally, the linewidths in the spectrum are enlarged significantly, showing that the contributions of the interband absorption (the losses in the metal) are magnified. Figure 8 shows the dramatic change in the evolution dynamics of the
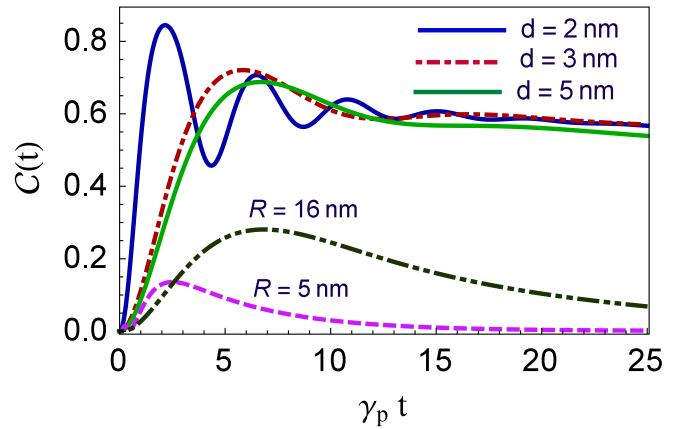
FIG. 8. The concurrence as a function of normalized time with varying the thickness of the nanoshell: $d = 2$ nm (solid blue curve), 3 nm (dash-dotted red curve), and 5 nm (solid green curve). Here, $h_a = 5$ nm and $h_b = 1$ nm from the surface of Au$_2$S/Ag. For comparison, the concurrence in the limit of the refractive index of the Au$_2$S core n_c and the refractive index of the silver shell $n_m(\omega)$ being equal is shown with different sizes: $R = 16$ nm (dash-double-dotted dark green curve) and $R = 5$ nm (dashed pink curve).

coupled QDs and subsequently the entanglement by varying the shell thickness while keeping the outer radius fixed at a certain value, namely, 16 nm. In addition, we have also considered the quantum entanglement in the limit of the refractive index of the Au$_2$S core n_c and the refractive index of the silver shell $n_m(\omega)$ being equal. This case represents a solid sphere with permittivity $\epsilon_m(\omega, R_1)$ embedded in a homogenous medium with dielectric constant ϵ_b. Here, we have calculated the concurrence for the solid sphere with two different sizes: $R = 16$ nm (dash-double-dotted dark green curve) and $R = 5$ nm (dashed pink curve). The results in Fig. 8 confirm that generating an efficient entanglement in the vicinity of a solid sphere is unlikely. Clearly, the realistic parameters that we used in the numerical calculations including the retardation effects and the inherent losses in the nanoparticle as elaborated in Fig. 2(b) indicate that the application of the nanoshell with a controllable shell thickness as well as the core material is advantageous over a solid sphere for creating pronounced entangled pairs from a one-QD excited initial condition.

IV. CONCLUSIONS

We have presented an applicable scheme that allows us to investigate quantum correlations between two single QDs in the proximity of a metal nanoshell. We used a self-consistent photon Green's function technique to explore the quantum optical and entanglement dynamics between two QDs that cover all the coupling regimes. In the vicinity of the nanoshell, the local density of states increased immensely, leading to the strong-coupling regime. The degree of the entanglement characterized by the concurrence can be maximized by optimizing the shell thickness as well as the ratio of the distances between the QDs and the surface of the shell. The loss of the system is greatly reduced even when the QDs are ultraclose to the shell, which signifies the slow decay rate of the coherence information and longtime entanglement preservation, which

is highly desirable for the quantum information science community. In addition, the population dynamics with solid-state QDs are found to have great flexibility in deriving a substantial amount of qubit entanglement in many cases and subsequently offer several advantages over coupling identical atoms. Our protocol allows for an on-demand, fast, and almost perfect entanglement even at strong carrier-phonon interaction where other systems fail. We noticed that the realistic parameters that we used, including the retardation effects and the inherent losses in the nanoparticle, are unlikely to generate an efficient entanglement in the vicinity of a solid sphere. There is also the potential to see strong coupling if one uses MNPs with nonspherical shapes, e.g., cigar shapes [46]. Rapid advances in nanofabrication techniques for plasmonic nanoparticles put such a system within experimental reach.

APPENDIX A: ELECTROMAGNETIC DYADIC GREEN'S FUNCTION IN SPHERICALLY THREE-LAYERED MEDIA

Given a spherical core of radius R_2 and dielectric constant ϵ_c surrounded by a concentric shell of radius R_1 and permittivity $\epsilon_m(\omega)$, embedded in a homogenous medium with dielectric constant ϵ_b, the dyadic Green's function is constructed from the expansion of the spherical vector wave function with the boundary conditions at the spherical interfaces satisfied [47]. If the source $\boldsymbol{r'}$ is outside the structure, the Green's function can be decomposed into $\boldsymbol{G}(\boldsymbol{r},\boldsymbol{r'},\omega) = \boldsymbol{G}^0(\boldsymbol{r},\boldsymbol{r'},\omega) + \boldsymbol{G}^{R(11)}(\boldsymbol{r},\boldsymbol{r'},\omega)$, where $\boldsymbol{G}^0(\boldsymbol{r},\boldsymbol{r'},\omega)$ is the direct contribution from the radiation sources in an unbounded medium and $\boldsymbol{G}^{R(11)}(\boldsymbol{r},\boldsymbol{r'},\omega)$ is the reflection contribution coming from the interaction of the emitter with the spherical nanoparticle. The direct term of the Green's function is given by [47]

$$\boldsymbol{G}^0(\boldsymbol{r},\boldsymbol{r'},\omega) = -\frac{\hat{\boldsymbol{r}}\hat{\boldsymbol{r}}\delta(\boldsymbol{r}-\boldsymbol{r'})}{k_1^2} + \frac{ik_1}{4\pi}\sum_{e,o}\sum_{n=1}^{\infty}\sum_{m=0}^{n}(2-\delta_{0m})\frac{2n+1}{n(n+1)}\frac{(n-m)!}{(n+m)!}\begin{cases}\boldsymbol{M}_{mn_o^e}^{(1)}(\boldsymbol{r},k_1)\boldsymbol{M}_{mn_o^e}(\boldsymbol{r'},k_1)+\boldsymbol{N}_{mn_o^e}^{(1)}(\boldsymbol{r},k_1)\boldsymbol{N}_{mn_o^e}(\boldsymbol{r'},k_1)\\ \boldsymbol{M}_{mn_o^e}(\boldsymbol{r},k_1)\boldsymbol{M}_{mn_o^e}^{(1)}(\boldsymbol{r'},k_1)+\boldsymbol{N}_{mn_o^e}(\boldsymbol{r},k_1)\boldsymbol{N}_{mn_o^e}^{(1)}(\boldsymbol{r'},k_1),\end{cases}$$

$$(A1)$$

where the upper (lower) line holds for $\boldsymbol{r} > \boldsymbol{r'}(\boldsymbol{r} < \boldsymbol{r'})$. For the scattered part [47]

$$\boldsymbol{G}^{R(11)}(\boldsymbol{r},\boldsymbol{r'},\omega) = \frac{ik_1}{4\pi}\sum_{e,o}\sum_{n=1}^{\infty}\sum_{m=0}^{n}(2-\delta_{0m})\frac{2n+1}{n(n+1)}\frac{(n-m)!}{(n+m)!}\left\{\mathcal{B}_M^{11}(\omega)\boldsymbol{M}_{mn_o^e}^{(1)}(\boldsymbol{r},k_1)\boldsymbol{M}_{mn_o^e}^{(1)}(\boldsymbol{r'},k_1) + \mathcal{B}_N^{11}(\omega)\boldsymbol{N}_{mn_o^e}^{(1)}(\boldsymbol{r},k_1)\boldsymbol{N}_{mn_o^e}^{(1)}(\boldsymbol{r'},k_1)\right\},$$

$$(A2)$$

where the prime denotes the coordinates (r',θ',φ') of the current source, m and n identify the eigenvalue parameters, and $\boldsymbol{M}_{mn_o^e}$ stands for the electric field of the TE$_{mn}$ mode, while $\boldsymbol{N}_{mn_o^e}$ represents that of the TM$_{mn}$ mode. Here, $k_1 = \frac{\omega}{c}\sqrt{\epsilon_b}$, $k_2 = \frac{\omega}{c}\sqrt{\epsilon_m(\omega)}$, and $k_3 = \frac{\omega}{c}\sqrt{\epsilon_c}$. The spherical vector wave functions are given by

$$\boldsymbol{M}_{mn}^e(\boldsymbol{r},k) = -\frac{m}{\sin\theta}j_n(kr)P_n^m(\cos\theta)\sin m\varphi\hat{\boldsymbol{\theta}} - j_n(kr)\frac{dP_n^m(\cos\theta)}{d\theta}\cos m\varphi\hat{\boldsymbol{\varphi}},$$

$$(A3)$$

$$\boldsymbol{M}_{mn}^o(\boldsymbol{r},k) = \frac{m}{\sin\theta}j_n(kr)P_n^m(\cos\theta)\cos m\varphi\hat{\boldsymbol{\theta}} - j_n(kr)\frac{dP_n^m(\cos\theta)}{d\theta}\sin m\varphi\hat{\boldsymbol{\varphi}},$$

$$(A4)$$

$$\boldsymbol{N}_{mn}^e(\boldsymbol{r},k) = \frac{n(n+1)}{kr}j_n(kr)P_n^m(\cos\theta)\cos m\varphi\hat{\boldsymbol{r}} + \frac{1}{kr}\frac{d[rj_n(kr)]}{dr}\frac{dP_n^m(\cos\theta)}{d\theta}\cos m\varphi\hat{\boldsymbol{\theta}}$$
$$- \frac{m}{kr\sin\theta}\frac{d[rj_n(kr)]}{dr}P_n^m(\cos\theta)\sin m\varphi\hat{\boldsymbol{\varphi}},$$

$$(A5)$$

$$\boldsymbol{N}_{mn}^o(\boldsymbol{r},k) = \frac{n(n+1)}{kr}j_n(kr)P_n^m(\cos\theta)\sin m\varphi\hat{\boldsymbol{r}} + \frac{1}{kr}\frac{d[rj_n(kr)]}{dr}\frac{dP_n^m(\cos\theta)}{d\theta}\sin m\varphi\hat{\boldsymbol{\theta}} + \frac{m}{kr\sin\theta}\frac{d[rj_n(kr)]}{dr}P_n^m(\cos\theta)\cos m\varphi\hat{\boldsymbol{\varphi}},$$

$$(A6)$$

where P_n^m are the associated Legendre polynomials and j_n are the spherical Bessel functions. The superscript (1) in Eqs. (A1) and (A2) indicates that in these equations, the spherical Bessel function $j_n(x)$ has to be replaced by the spherical Hankel function of the first kind $h_n^{(1)}(x)$. The coefficients $\mathcal{B}_M^{11}$ and $\mathcal{B}_N^{11}$ in the full Green's function (A2) can be determined by imposing the boundary conditions at the surfaces $r = R_1$ and $r = R_2$.

$$\boldsymbol{r} \times \boldsymbol{G}(\boldsymbol{r},\boldsymbol{r'})_{r=R^-} = \boldsymbol{r} \times \boldsymbol{G}(\boldsymbol{r},\boldsymbol{r'})_{r=R^+},$$

$$(A7)$$

$$\boldsymbol{r} \times \boldsymbol{\nabla} \times \boldsymbol{G}(\boldsymbol{r},\boldsymbol{r'})_{r=R^-} = \boldsymbol{r} \times \boldsymbol{\nabla} \times \boldsymbol{G}(\boldsymbol{r},\boldsymbol{r'})_{r=R^+}.$$

$$(A8)$$

The resulting expressions for the coefficients are

$$\mathcal{B}_M^{11}(\omega) = -\frac{k_2\Im_{11}\big[\partial\Im_{21} - \partial\hbar_{21}\mathcal{R}_M^{11}(\omega)\big] - k_1\partial\Im_{11}\big[\Im_{21} - \hbar_{21}\mathcal{R}_M^{11}(\omega)\big]}{k_2\hbar_{11}\big[\partial\Im_{21} - \partial\hbar_{21}\mathcal{R}_M^{11}(\omega)\big] - k_1\partial\hbar_{11}\big[\Im_{21} - \hbar_{21}\mathcal{R}_M^{11}(\omega)\big]}, \tag{A9}$$

$$\mathcal{B}_N^{11}(\omega) = -\frac{k_2\partial\Im_{11}\big[\Im_{21} - \hbar_{21}\mathcal{R}_N^{11}(\omega)\big] - k_1\Im_{11}\big[\partial\Im_{21} - \partial\hbar_{21}\mathcal{R}_N^{11}(\omega)\big]}{k_2\partial\hbar_{11}\big[\Im_{21} - \hbar_{21}\mathcal{R}_N^{11}(\omega)\big] - k_1\hbar_{11}\big[\partial\Im_{21} - \partial\hbar_{21}\mathcal{R}_N^{11}(\omega)\big]}, \tag{A10}$$

where

$$\mathcal{R}_M^{11}(\omega) = \frac{k_3\Im_{22}\partial\Im_{32} - k_2\Im_{32}\partial\Im_{22}}{k_3\hbar_{22}\partial\Im_{32} - k_2\Im_{32}\partial\hbar_{22}}, \tag{A11}$$

$$\mathcal{R}_N^{11}(\omega) = \frac{k_3\Im_{32}\partial\Im_{22} - k_2\Im_{22}\partial\Im_{32}}{k_3\Im_{32}\partial\hbar_{22} - k_2\hbar_{22}\partial\Im_{32}}, \tag{A12}$$

with

$$\Im_{il} = j_n(k_i R_l), \tag{A13}$$

$$\hbar_{il} = h_n^{(1)}(k_i R_l), \tag{A14}$$

$$\partial\Im_{il} = \frac{1}{\rho}\frac{d[\rho j_n(\rho)]}{d\rho}\bigg|_{\rho=k_i R_l}, \tag{A15}$$

$$\partial\hbar_{il} = \frac{1}{\rho}\frac{d\big[\rho h_n^{(1)}(\rho)\big]}{d\rho}\bigg|_{\rho=k_i R_l}. \tag{A16}$$

APPENDIX B: EIGENFREQUENCY RELATION

The plasmon resonance can be obtained by including the retardation effect from the explicit form of the reflection coefficients derived in Appendix A by noticing that these coefficients contain poles at the points where the denominator vanishes. These poles give the eigenfrequency relation of the electric modes supported by the metallic shell:

$$h_n^{(1)}(\rho_1)\alpha_n = \big[\rho_1 h_n^{(1)}(\rho_1)\big]'\beta_n, \tag{B1}$$

where

$$\alpha_n = k_2^2[\rho_2 j_n(\rho_2)]' A_n - k_3^2 j_n(\rho_2) B_n, \tag{B2}$$

$$\beta_n = \frac{k_2^2}{k_1^2}\big\{k_2^2[\rho_2 j_n(\rho_2)]' C_n - k_3^2 j_n(\rho_2) D_n\big\}, \tag{B3}$$

with

$$A_n = j_n(\eta_2)\big[\eta_1 h_n^{(1)}(\eta_1)\big]' - h_n^{(1)}(\eta_2)[\eta_1 j_n(\eta_1)]', \tag{B4}$$

$$B_n = \big[\eta_1 h_n^{(1)}(\eta_1)\big]'[\eta_2 j_n(\eta_2)]' - \big[\eta_2 h_n^{(1)}(\eta_2)\big]'[\eta_1 j_n(\eta_1)]', \tag{B5}$$

$$C_n = j_n(\eta_2)h_n^{(1)}(\eta_1) - j_n(\eta_1)h_n^{(1)}(\eta_2), \tag{B6}$$

$$D_n = h_n^{(1)}(\eta_1)[\eta_2 j_n(\eta_2)]' - j_n(\eta_1)[\eta_2 h_n^{(1)}(\eta_2)]', \tag{B7}$$

where $\rho_1 = k_1 R_1$, $\rho_2 = k_3 R_2$, $\eta_1 = k_2 R_1$, $\eta_2 = k_2 R_2$, and the prime denotes differentiation with respect to the argument. Here, $k_1 = \frac{\omega}{c}\sqrt{\epsilon_b}$, $k_2 = \frac{\omega}{c}\sqrt{\epsilon_m(\omega)}$, and $k_3 = \frac{\omega}{c}\sqrt{\epsilon_c}$.

[1] D. E. Chang, A. S. Sorensen, P. R. Hemmer, and M. D. Lukin, Phys. Rev. Lett. **97**, 053002 (2006).

[2] D. E. Chang, A. S. Sorensen, E. A. Demler, and M. D. Lukin, Nat. Phys. **3**, 807 (2007).

[3] J. Hakami, L. Wang, and M. S. Zubairy, Phys. Rev. A **89**, 053835 (2014).

[4] A. Delga, J. Feist, J. Bravo-Abad, and F. J. Garcia-Vidal, Phys. Rev. Lett. **112**, 253601 (2014).

[5] A. Ridolfo, O. Di Stefano, N. Fina, R. Saija, and S. Savasta, Phys. Rev. Lett. **105**, 263601 (2010).

[6] Y. Gu, L. Huang, O. J. F. Martin, and Q. Gong, Phys. Rev. B **81**, 193103 (2010).

[7] A. V. Akimov, A. Mukherjee, C. L. Yu, D. E. Chang, A. S. Zibrov, P. R. Hemmer, H. Park, and M. D. Lukin, Nature (London) **450**, 402 (2007).

[8] T. Torimoto, H. Horibe, T. Kameyama, K. Okazaki, S. Ikeda, M. Matsumura, A. Ishikawa, and H. Ishihara, J. Phys. Chem. Lett. **2**, 2057 (2011).

[9] A. Ishikawa, K. Osono, A. Nobuhiro, Y. Mizumoto, T. Torimoto, and H. Ishihara, Phys. Chem. Chem. Phys. **15**, 4214 (2013).

[10] K. Cho, *Optical Response of Nanostructures* (Springer, Berlin, 2003).

[11] S. Hughes, Phys. Rev. Lett. **95**, 257403 (2005).

[12] L. A. Webster, K. Truex, L.-M. Duan, D. G. Steel, A. S. Bracker, D. Gammon, and L. J. Sham, Phys. Rev. Lett. **112**, 126801 (2014).

[13] M. L. Andersen, S. Stobbe, A. S. Sørensen, and P. Lodahl, Nature (London) **7**, 215 (2011).

[14] D. Kim, S. G. Carter, A. Greilich, A. S. Bracker, and D. Gammon, Nature (London) **7**, 223 (2011).

[15] X. Li, Y. Wu, D. Steel, D. Gammon, T. H. Stievater, D. S. Katzer, D. Park, C. Piermarocchi, and L. J. Sham, Science **301**, 809 (2003).

[16] Y. He and K.-D. Zhu, Nano. Res. Lett. **7**, 95 (2012).

[17] K. V. Nerkararyan and S. I. Bozhevolnyi, Phys. Rev. B **92**, 045410 (2015).

[18] E. Prodan, C. Radloff, N. J. Halas, and P. Nordlander, Science **302**, 419 (2003).

[19] S. A. Maier, *Plasmonics: Fundamental and Applications* (Springer, New York, 2007).

[20] H. A. Atwater, Sci. Am. **17**, 56 (2007).

[21] R. D. Averitt, D. Sarkar, and N. J. Halas, Phys. Rev. Lett. **78**, 4217 (1997).

[22] P. B. Johnson and R. W. Christy, Phys. Rev. B **6**, 4370 (1972).

[23] A. Zrenner, E. Beham, S. Stufler, F. Findeis, M. Bichler, and G. Abstreiter, Nature (London) **418**, 612 (2002).

[24] E. B. Flagg, A. Muller, J. W. Robertson, S. Founta, D. G. Deppe, M. Xiao, W. Ma, G. J. Salamo, and C. K. Shih, Nature (London) **5**, 203 (2009).

[25] D. Gammon and D. G. Steel, Phys. Today **55**(10), 36 (2002).

[26] T. Yoshie, A. Scherer, J. Hendrickson, G. Khitrova, H. M. Gibbs, G. Rupper, C. Ell, O. B. Shchekin, and D. G. Deppe, Nature (London) **432**, 200 (2004).

[27] C. V. Vlack, P. T. Kristensen, and S. Hughes, Phys. Rev. B **85**, 075303 (2012).

[28] J. M. Villas-Bôas, S. E. Ulloa, and A. O. Govorov, Phys. Rev. Lett. **94**, 057404 (2005).

[29] U. Kreibig and M. Vollmer, *Optical Properties of Metal Clusters* (Springer, Berlin, 1995).

[30] J. A. Scholl, S. Stobbe, A. L. Koh, and J. A. Dionne, Nature (London) **483**, 421 (2012).

[31] H. T. Dung, S. Y. Buhmann, L. Knöll, D.-G. Welsch, S. Scheel, and J. Köstel, Phys. Rev. A **68**, 043816 (2003).

[32] K. J. Ahn and A. Knorr, Phys. Rev. B **68**, 161307(R) (2003).

[33] S. Stobbe, P. T. Kristensen, J. E. Mortensen, J. M. Hvam, J. Mørk, and P. Lodahl, Phys. Rev. B **86**, 085304 (2012).

[34] J. R. Zurita-Sánchez and L. Novotny, J. Opt. Soc. Am. B **19**, 1355 (2002).

[35] P. T. Kristensen, J. E. Mortensen, P. Lodahl, and S. Stobbe, Phys. Rev. B **88**, 205308 (2013).

[36] W. H. Press, S. A. Teukolsky, W. T. Vetterling, and B. P. Flanery, *Numerical Recipes in FORTRAN: The Art of Scientific Computing* (Cambridge University Press, Cambridge, 1992).

[37] L. Novotny and B. Hecht, *Principles of Nano-optics* (Cambridge University Press, Cambridge, 2012).

[38] R. S. Savelev, A. P. Slobozhanyuk, A. E. Miroshnichenko, Y. S. Kivshar, and P. A. Belov, Phys. Rev. B **89**, 035435 (2014).

[39] M. A. Noginov, G. Zhu, A. M. Belgrave, R. Bakker, V. M. Shalaev, E. E. Narimanov, S. Stout, E. Herz, T. Suteewong, and U. Wiesner, Nature (London) **460**, 1110 (2009).

[40] K. T. Butler, P. E. Vullum, A. M. Muggerud, E. Cabrera, and J. H. Harding, Phys. Rev. B **83**, 235307 (2011).

[41] R. Bardhan, N. K. Grady, T. Ali, and N. J. Halas, ACS Nano **4**, 6169 (2010).

[42] T. Unold, K. Mueller, C. Lienau, T. Elsaesser, and A. D. Wieck, Phys. Rev. Lett. **94**, 137404 (2005).

[43] S. Weiler, A. Ulhaq, S. M. Ulrich, D. Richter, M. Jetter, P. Michler, C. Roy, and S. Hughes, Phys. Rev. B **86**, 241304(R) (2012).

[44] H. Qiao, K. A. Abel, F. C. J. M. van Veggel, and J. F. Young, Phys. Rev. B **82**, 165435 (2010).

[45] W. K. Wootters, Phys. Rev. Lett. **80**, 2245 (1998).

[46] A. Trügler and U. Hohenester, Phys. Rev. B **77**, 115403 (2008).

[47] L.-W. Li, P.-S. Kooi, M.-S. Leong, and T.-S. Yee, IEEE Trans. Microwave Theory Tech. **42**, 2302 (1994).